Optics Letters

Optimal bandwidth micropolarizer arrays

ANDREY S. ALENIN[1,*], ISRAEL J. VAUGHN[1], AND J. SCOTT TYO[1]

[1]School of Engineering and Information Technology, University of New South Wales, Canberra, ACT 2610, Australia
[*]Corresponding author: a.alenin@adfa.edu.au

Compiled December 14, 2017

Currently, the best performing micropolarizer array is the 2×4 pattern introduced by LeMaster and Hirakawa. In this Letter, we extend the available set of patterns with the aim of improving reconstruction quality by leveraging the Fourier domain and designing information carriers that yield optimal bandwidth. First, the family of $2 \times L$ patterns widens the optimization space of the 2×4 pattern by facilitating variable allocation of bandwidth for channels surrounding polarization and intensity carriers. Second, the $2 \times 2 \times N$ patterns present an intriguing option for use within a hybrid spatiotemporal modulation scheme, where the multiple temporal measurements enable maximum theoretical spatial resolution of reconstructed Stokes parameters.

OCIS codes: (110.5405) Polarimetric imaging; (260.5430) Polarization; (120.5410) Polarimetry

http://dx.doi.org/10.1364/OL.xx.xxxxxx

Recent improvements in manufacturing have made the class of division of focal plane (DoFP) polarimeters [1] more competitive with other polarimeter classes. The first successful micropolarizer array (MPA) was introduced by Chun [2] in 1994 and has become colloquially known as the microgrid polarimeter. Despite its prevalence, the engineering considerations at the time did not include the now more widely acknowledged significance of maximizing bandwidth within the Fourier domain. These principles were pioneered for polarimeters by Tyo, LaCasse, and colleagues [3–5], while the first attempt to build upon the conventional MPA was undertaken by LeMaster and Hirakawa [6]. They demonstrated improved reconstruction quality in both s_0 and degree of linear polarization (DoLP) when using their 2×4 MPA rather than the conventional 2×2 MPA. In this Letter, we generalize the interaction of MPA design in terms of the bandwidth provided and the reconstruction quality achieved.

The Stokes vector [1],

$$\begin{aligned}\underline{\mathbf{S}} &= \begin{bmatrix} s_0 & s_1 & s_2 & s_3 \end{bmatrix}^{\mathrm{T}} \\ &= \begin{bmatrix} I_H + I_V & I_H - I_V & I_{+45} - I_{-45} & I_R - I_L \end{bmatrix}^{\mathrm{T}}, \end{aligned} \tag{1}$$

is a common way to describe the polarization of incoherent light. The latter three parameters represent differential irradiance measurements and are constrained to lie inside the Poincaré sphere, $s_0 \geqslant \sqrt{s_1^2 + s_2^2 + s_3^2}$. To measure Stokes parameters, indirect measurements are made by passing light of an unknown polarization state, $\underline{\mathbf{S}}$, through a series of predetermined analyzing polarization states, $\underline{\mathbf{A}}_n$. By grouping N measurements together,

$$\begin{aligned}\underline{\mathbf{I}} &= \begin{bmatrix} I_1 & \cdots & I_N \end{bmatrix}^{\mathrm{T}} \\ &= \begin{bmatrix} \underline{\mathbf{A}}_1^{\mathrm{T}}\underline{\mathbf{S}} & \cdots & \underline{\mathbf{A}}_N^{\mathrm{T}}\underline{\mathbf{S}} \end{bmatrix}^{\mathrm{T}} + \vec{\mathbf{n}} = \underline{\underline{\mathbf{W}}}\underline{\mathbf{S}} + \vec{\mathbf{n}}, \end{aligned} \tag{2}$$

the data can then be manipulated to reveal the unknown state's Stokes parameters by calculating the pseudo-inverse, $\underline{\underline{\mathbf{W}}}^+$, and applying the Data Reduction Method (DRM),

$$\hat{\underline{\mathbf{S}}} = \underline{\underline{\mathbf{W}}}^+\underline{\mathbf{I}} = \underline{\underline{\mathbf{W}}}^+\underline{\underline{\mathbf{W}}}\underline{\mathbf{S}} + \underline{\underline{\mathbf{W}}}^+\vec{\mathbf{n}}, \tag{3}$$

where $\vec{\mathbf{n}}$ represents additive detector noise.

The conventional MPA aligns polarizers at 0°, +45°, 90° and −45° in a 2×2 pattern that can be seen in Fig. 1A, and the (m, n)th pixel has the following analyzing vector,

$$\underline{\mathbf{A}}_{m,n} = \frac{1}{4}\begin{bmatrix} 2 \\ \cos(m\pi) + \cos(n\pi) \\ \cos(m\pi) - \cos(n\pi) \end{bmatrix}, \tag{4}$$

where $a_3 = 0$ and is omitted for brevity. Because each of the four pixels observe a slightly different $\underline{\mathbf{S}}$, applying DRM directly onto intensities in Eq. (1) leads to instantaneous field-of-view (IFOV) errors [7]. Tyo [3] and LaCasse [4, 5] showed that by transforming to the Fourier domain of the raw microgrid image, it is possible to extract the polarization information with better aliasing performance. Extending their work, LeMaster and Hirakawa [6] proposed a 2×4 MPA shown in Fig. 1B. A permutation of that pattern belongs to the family,

$$\underline{\mathbf{A}}_{m,n} = \frac{1}{2}\begin{bmatrix} 1 \\ \cos(am\pi)\cos(bn\pi) \\ \sin(am\pi)\cos(bn\pi) \end{bmatrix}, \tag{5}$$

where a and b are the carrier frequencies in x and y, respectively, in cycles per pixel. LeMaster's MPA satisfies Eq. (5) with $a = 1/2$ and $b = 1$. Two additional members shown in Figs. 1C and 1D will be discussed in greater detail.

Since DoFP polarimeters rely on periodically oriented micropolarizers, it is appropriate to treat such systems within the Fourier domain. To examine the channel structure, we adapt our $\underline{\mathbf{Q}}$ formalism [8] to Stokes polarimeters. We expand I_n from

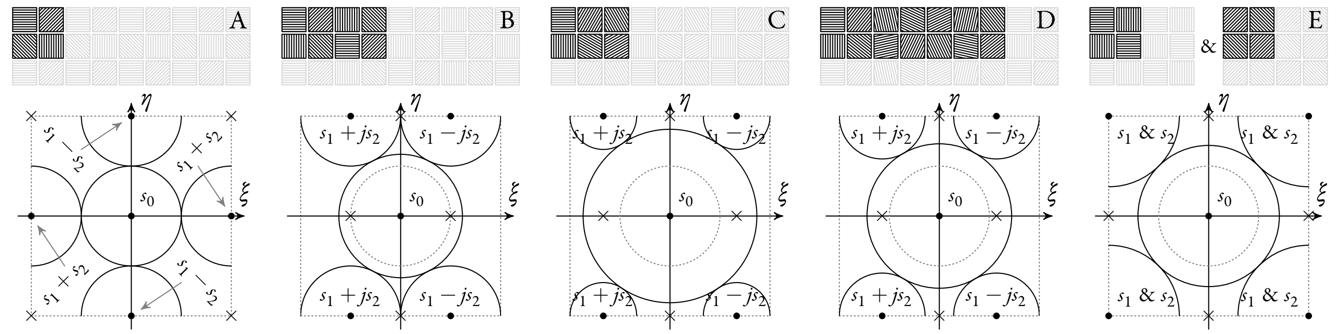

Fig. 1. MPAs. Top row: (A) Conventional 2×2, (B) LeMaster's 2×4, (C) This work's 2×3, (D) This work's 2×7, (E) This work's $2 \times 2 \times 2$. Bottom row: Fourier domains with $\bullet/\times$ indicating channel centers for filled and empty channels, respectively, as contained within $\underline{\tilde{\mathbf{A}}}$ of Eq. (8) for $2 \times L$ MPAs; solid lines outline the allocated channel bandwidths, while dotted lines outline the allocated s_0 bandwidth of the conventional MPA.

Table 1. Notable Micropolarizer Array Patterns[a]

Origin	Size	a	b	N	CN	$\sigma^2_{0,1,2,3}$	$\underline{\mathbf{Q}}^{\mathrm{T}}$	$\underline{\mathbf{Q}}^{+}$
Chun [2]	2×2	–	–	1	$\sqrt{2}$	$1, 4, 4, \varnothing$	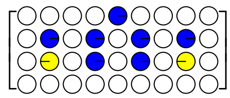	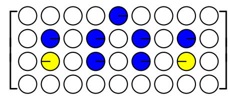
LeMaster [6]	2×4	$1/2$	1	1	$\sqrt{2}$	$1, 4, 4, \varnothing$	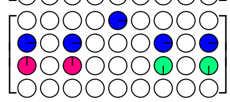	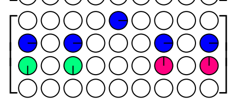
This Work	2×3	$2/3$	1	1	$\sqrt{2}$	$1, 4, 4, \varnothing$		
This Work	2×7	$4/7$	1	1	$\sqrt{2}$	$1, 4, 4, \varnothing$		
				1	$\sqrt{1}$	$1, 4, \varnothing, \varnothing$	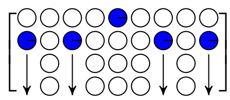	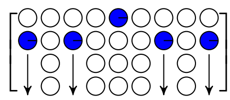
This Work	$2 \times 2 \times N$	1	1	2	$\sqrt{2}$	$\frac{1}{2}, 4, 4, \varnothing$		
				3	$\sqrt{3}$	$\frac{1}{3}, 4, 4, 4$		

[a]CN is the condition number of the unit-cell's $\underline{\mathbf{W}}$. $\sigma^2_{0,1,2,3}$ are the noise variances for each Stokes parameter from $\underline{\mathbf{Q}}$; their sum is EWV ($\varnothing$ is unreconstructable). The circles represent the polar form of the coefficients—the direction of the radius line contains the phase information as: right= +1, up= +j, left= −1, down= −j. Empty circles indicate that a given Stokes parameter is not contained within a given channel; a vertical set of circles in $\underline{\mathbf{Q}}^{\mathrm{T}}$ and $\underline{\mathbf{Q}}^{+}$ denotes an empty channel.

Eq. (2) into a sampled 2D scene, $I(x, y)$. The Fourier transform, $\tilde{I}(\xi, \eta)$, can be divided into a set of channels, $\mathcal{F}\{\underline{\mathbf{C}}\}$, which are related to the four Stokes parameters through $\underline{\mathbf{Q}}$,

$$\mathcal{F}\{\underline{\mathbf{C}}\} = \underline{\mathbf{Q}}\mathcal{F}\{\underline{\mathbf{S}}\} = \left[\ \mathbf{q}_{\xi,\eta;s_0} \quad \mathbf{q}_{\xi,\eta;s_1} \quad \mathbf{q}_{\xi,\eta;s_2} \quad \mathbf{q}_{\xi,\eta;s_3}\ \right]\mathcal{F}\{\underline{\mathbf{S}}\}, \tag{6}$$

where $\mathbf{q}_{\xi,\eta;s_i}$ is the channel structure for each Stokes parameter. Their concatenation maps information into the set of carriers afforded by a given MPA design. By properly keeping track of this mapping and inverting the process, we can reconstruct $\underline{\mathbf{S}}$,

$$\hat{\underline{\mathbf{S}}} = \mathcal{F}^{-1}\left\{\underline{\mathbf{Q}}^{+}\mathcal{F}\{\underline{\mathbf{C}}\}\right\}, \tag{7}$$

where $\underline{\mathbf{Q}}^{+}$ is the pseduo-inverse. As was shown in our original work, the Frequency Phase Matrix can readily reveal the Fourier transform of Eq. (5) and thereby describe the corresponding channel structure of every member of the family,

$$\tilde{\underline{\mathbf{A}}}_{m,n} = \begin{bmatrix} \frac{1}{2}\delta(\xi, \eta) \\ \frac{1}{8}\left[+\delta(\xi - \frac{a}{2}, \eta \pm \frac{b}{2}) + \delta(\xi + \frac{a}{2}, \eta \pm \frac{b}{2})\right] \\ \frac{j}{8}\left[-\delta(\xi - \frac{a}{2}, \eta \pm \frac{b}{2}) + \delta(\xi + \frac{a}{2}, \eta \pm \frac{b}{2})\right] \end{bmatrix}. \tag{8}$$

Eq. (8) depicts the channel structure with nine channels centered at $(\{-a/2, 0, +a/2\}, \{-b/2, 0, +b/2\})$. The resulting measurement and its reconstruction can be performed with $\underline{\mathbf{Q}}$ and its inverse shown in Table 1. Because the s_0 channel is at baseband, while s_1 and s_2 have exactly two carriers—one in x and one in y—it follows that all MPAs have four empty channels, while utilizing the remaining five.

Minimizing equally weighted variance (EWV) is correlated with making channels more independent [8]. Intuitively, this makes sense—if you want to retain noise resilience, mix information less. Thus, if noise resilience was the primary requirement for an MPA, the "optimal" configuration would set a or b to zero, thereby removing either the x- or the y-carrier, respectively. That would result in a $1 \times L$ MPA with three channels, and applying the fact that each sinusoidal modulation doubles the variance [8], the EWV for such MPAs would equal $1+2+2 = 5$. However, to maximize information bandwidth, a "non-optimal" modulation is more interesting. MPAs that have both x and y carriers sacrifice the ease of unmixing in favor of a significant increase in the separation of the channels carrying s_0 and s_1/s_2 information. This trade-off carries the penalty of increasing EWV to $1 + 4 + 4 = 9$, but the higher bandwidth of each channel leads to a more accurate reconstruction overall [5]: if the scene is very low bandwidth, the reconstruction is sufficient with channel centers; as the bandwidth increases, the reconstruction benefits from inclusion of higher frequencies. More generally, these considerations represent an overall need for a balanced approach to noise, bandwidth and system error [9]. Nonetheless, $1 \times L$ MPAs may be interesting in special cases—such as when the data is guaranteed to have significantly higher

Table 2. MPA parametrization

K	$\ell \geqslant 2$	L	a	b	$\sigma^2_{0,1,2,3}$	CN
1	even	2ℓ	$\frac{\ell-1-2p}{\ell}$	0	$1,2,2,\varnothing$	$\sqrt{2}$
	odd	ℓ				
2	even	2ℓ	$\frac{\ell-1-2p}{\ell}$	1	$1,4,4,\varnothing$	
	odd	ℓ				

frequencies in one of the spatial dimensions, or in push-broom systems. Table 2 parametrizes $1 \times L$ and $2 \times L$ families. The additional parameter, $p = \{0, 1, \ldots, \lceil \ell/2 \rceil - 1\}$, is an integer that allows discrete selection of carrier frequency between 0 and $(\ell - 1)/\ell$. For example, the 2×7 MPA can have $p = \{0, 1, 2\}$, which corresponds to $a = \{6/7, 4/7, 2/7\}$. For the data in Fig. 2, MPAs with $a \sim 0.6$ proved most interesting. Hence the choice of $p = 1$ and $a = 4/7$ for the 2×7 MPA in Fig. 1D.

It is possible to take a and b to the limit of both being equal to unity, which can be seen in Fig. 1E. This MPA extends the channel centers to the outer corners, which provides maximum possible bandwidth, but because $\sin(m\pi) = 0$ for $m \in \mathbb{Z}$, this MPA can only reconstruct s_0 and s_1. To obtain s_2, we can add a temporally modulated ferroelectric liquid crystal rotator, which can be modeled as a switching half-or-zero-wave plate oriented at $\vartheta = 22.5°$. This will effectively rotate each pixel by 45° between the two successive frames. To obtain s_3 as well, we can instead add a $\delta = 141.7°$ retarder and temporally cycle it through three orientations, $\vartheta = \{-56.2°, -30.0°, +46.4°\}$. These systems fit the previously introduced multi-snapshot channeled polarimeter nomenclature, but here we refer to them as $2 \times 2 \times N$ MPAs for brevity. To be fair in comparisons with other MPAs, special care is required—the exposure time needs to be split into N parts, and each one of them needs to receive a noise contribution with the variance scaled by $1/N$.

We simulated DoFP reconstruction with data from Ground MSPI [10] shown in Fig. 2. Since Ground MSPI is a division of time polarimeter, its data lacks spatial artifacts. Images were cropped to 1092×1092 to ensure that each of the MPA's unit-cells were included an integer number of times. This affixed the carriers to pixel boundaries within the Fourier domain and alleviated the need for any subsampling. For 16 independent instantiations of each noise level between 9dB and 36dB in mean signal-to-noise ratio (SNR), we perform two genetic algorithm optimizations: a) four parameters, $\{r_{\text{base}}, r_{\text{side}}, \varepsilon_{\text{base}}, \varepsilon_{\text{side}}\}$, defining filters to maximize DoLP accuracy; b) two parameters, $\{r_{\text{base}}, \varepsilon_{\text{base}}\}$, defining filters to maximize s_0 accuracy. We quantify accuracy with peak signal-to-noise ratio (PSNR) [11], which is related to mean squared error (MSE) as,

$$\text{PSNR} = 10\log_{10}\left(\text{MAX}^2/\text{MSE}\right), \quad (9)$$

where MAX = 1 for normalized s_0 and DoLP. The respective r and ε parameters define the Planck-Taper envelope: unity near the center, zero on the outside and the falloff range defined as

$$H(\varepsilon_i r_i \leqslant r \leqslant r_i) = \frac{1}{1 + \exp\left(-2\varepsilon_i r_i \left[\frac{1}{r - \varepsilon_i r_i} + \frac{1}{r - r_i}\right]\right)}. \quad (10)$$

Selecting the hyperplane $r_{\text{base}} + \varepsilon_{\text{base}} = r_{\text{side}} + \varepsilon_{\text{side}} = 1$ as the initial population constraint was found to produce the fastest convergence. Figure 4 shows reconstructed and absolute error images for a single noise instantiation of the 50 that were averaged to achieve the final accuracy results shown in Fig. 3.

For low SNRs, the MPA choice is irrelevant—the filters around each carrier are similarly sized as the outer regions of the Fourier domain are below the noise floor. As SNR increases, the filters widen for all MPAs, but do so at different rates. This rate is determined by two factors: a) the proximity of nearby carriers; b) information channel amplitude compared to the noise floor. It is in between these two factors that most gains are made (between 18dB and 30dB). As SNR reaches a high enough level, the reconstruction quality plateaus. At this point, further widening of filters is detrimental, since high frequency content from adjacent channels leads to crosstalk.

Overall, the 2×2 MPA yields the worst performance, while the $2 \times 2 \times 2$ MPA yields the best performance. However, there are engineering challenges associated with implementing the required hybrid modulation, and if its addition is impractical for a given application, the $2 \times L$ family is likely to provide the most compelling design. Figures 3 and 4 indicate that 2×3, 2×4 and 2×7 are all competitive and offer different trade-offs of s_0 and DoLP accuracy. Of the three, the 2×3 provides the best s_0 accuracy and the worst DoLP accuracy, while the 2×7 MPA outperforms LeMaster's 2×4 in both. Because the filter parameters were chosen to maximize reconstruction quality, the fact that the 2×7 provides a better trade-off between carrier separation and the allocated bandwidth than the 2×4,

Fig. 2. Ground MSPI data, $\lambda = 660$ nm. (A) s_0. (B) DoLP.

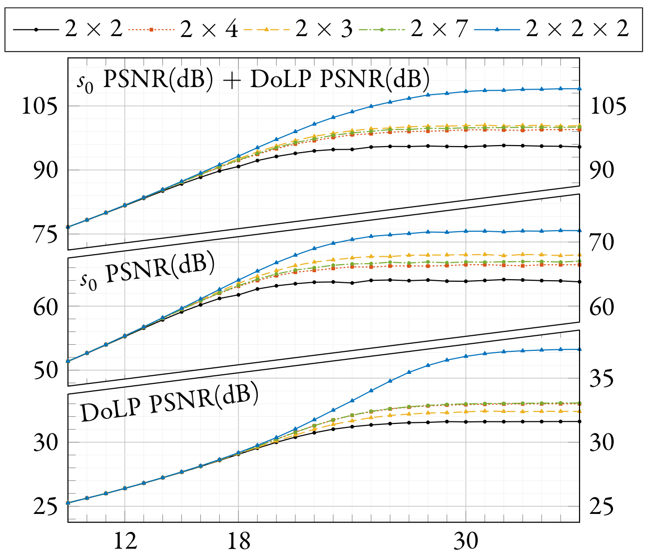

Fig. 3. Attainable reconstruction quality of MPAs in Fig. 1.

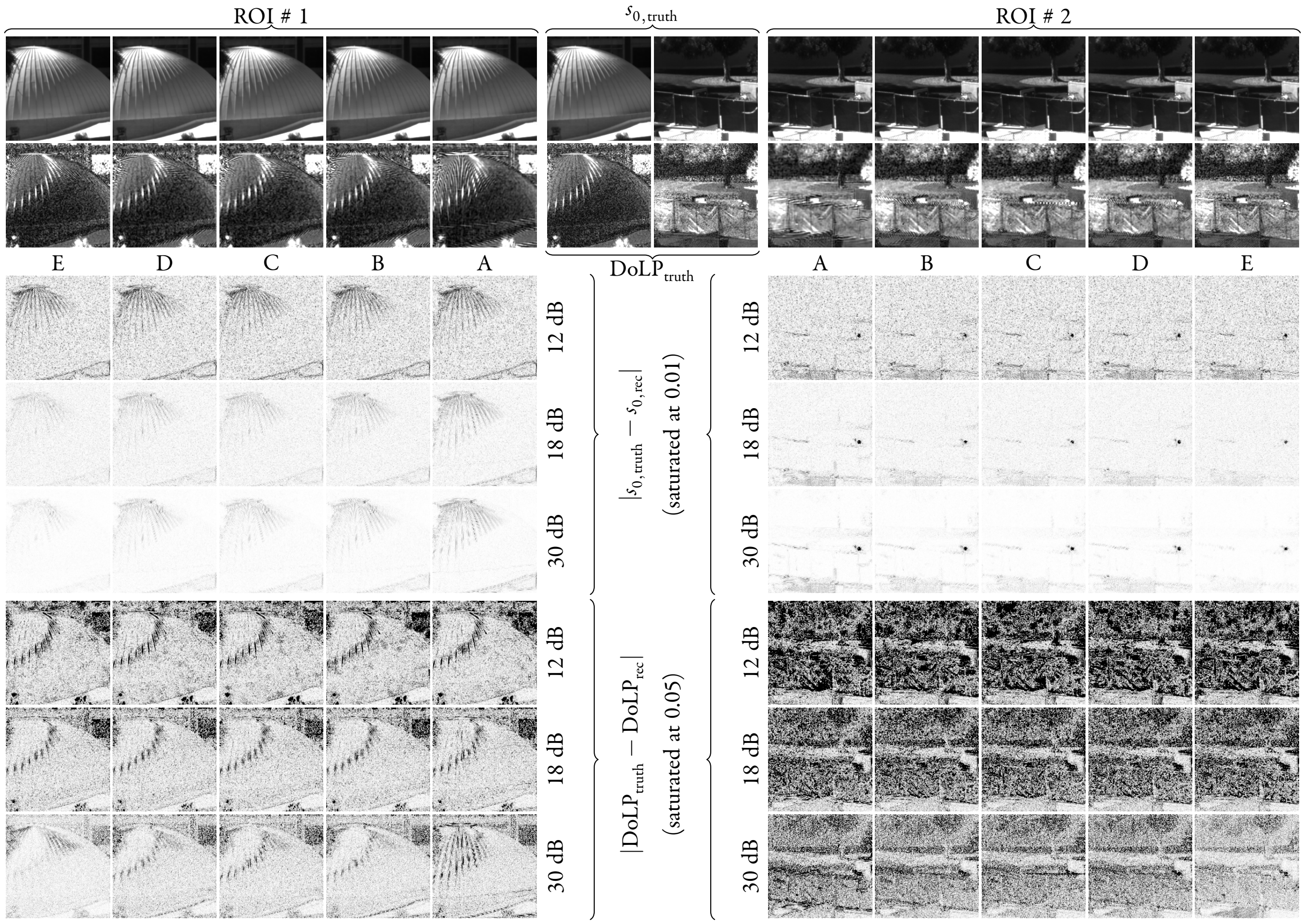

Fig. 4. Top two rows: the inside 2×2 grid shows the true s_0 and DoLP; the outside shows the reconstructed s_0 and DoLP at SNR = 30 dB. Bottom six rows: absolute error between reconstructed images and truth. MPA labels and ROIs are consistent with Figs. 1 and 2, respectively.

suggests that s_1 and s_2 channels may require less bandwidth than the s_0 channel. This is analogous to hyperspectral imaging, where it is well established that luminance information is generally of higher spatial bandwidth than chrominance information [12, 13]. Note that if s_1 and s_2 were of comparable bandwidth and magnitude to s_0, LeMaster's 2×4 would be the best MPA to use. Conversely, if s_1 and s_2 relative bandwidths were lower, the 2×3 would fare better. When designing an MPA for representative data, current state-of-the-art manufacturing capabilities make arbitrarily large L untenable. The likely error in polarizer orientations would have the effect of smearing a single carrier into a plurality of carriers along the top and bottom edges of the Fourier domain [14]. The resulting aliasing would make reconstruction excessively difficult, thereby negating the benefits of using the $\underline{\mathbf{Q}}$ formalism, while also exacerbating unit-cell locality and the associated IFOV errors that plague conventional DRM techniques. These constraints will diminish with time.

In this Letter, we have extended LeMaster's 2×4 MPA into a family of $2 \times L$ MPAs that allow for optimal carrier placement given the data. However, the improvement it brings is small in comparison to the one enabled by the $2 \times 2 \times N$ MPAs.

Funding. Asian Office of Aerospace Research and Development (FA2386-15-1-4098).

Acknowledgment. Data were provided by Christine Bradley and Russell Chipman from the University of Arizona.

REFERENCES

1. J. S. Tyo, D. L. Goldstein, D. B. Chenault, and J. A. Shaw, Appl. Opt. **45**, 5453 (2006).
2. C. S. L. Chun, D. L. Fleming, and E. J. Torok, Proc. SPIE **2234**, 275 (1994).
3. J. S. Tyo, C. F. LaCasse, and B. M. Ratliff, Opt. Lett. **34**, 3187 (2009).
4. C. F. LaCasse, R. A. Chipman, and J. S. Tyo, Opt. Express **19**, 14976 (2011).
5. C. F. LaCasse, J. S. Tyo, and R. A. Chipman, Opt. Lett. **37**, 1097 (2012).
6. D. A. LeMaster and K. Hirakawa, Opt. Lett. **39**, 1811 (2014).
7. B. M. Ratliff, C. F. LaCasse, and J. S. Tyo, Opt. Express **17**, 9112 (2009).
8. A. S. Alenin and J. S. Tyo, J. Opt. Soc. Am. A **31**, 1013 (2014).
9. J. S. Tyo, Appl. Opt. **41**, 619 (2002).
10. C. L. Bradley, M. Kupinski, D. J. Diner, F. Xu, and R. A. Chipman, Proc. SPIE **9613**, 96130U (2015).
11. Z. Wang and A. C. Bovik, IEEE Signal Process. Mag. **26**, 98 (2009).
12. D. Alleysson, S. Susstrunk and J. Herault, IEEE Trans. Image Process. **14**, 439 (2005).
13. E. Dubois, IEEE Signal Process. Lett. **12**, 847–850 (2005).
14. C. LaCasse, T. Ririe, R. Chipman, and J. S. Tyo, IEEE Aero. Conf. Proc. pp. 1–8 (2011).

REFERENCES

1. J. S. Tyo, D. L. Goldstein, D. B. Chenault, and J. A. Shaw, "Review of passive imaging polarimetry for remote sensing applications," Appl. Opt. **45**, 5453–5469 (2006).
2. C. S. L. Chun, D. L. Fleming, and E. J. Torok, "Polarization-sensitive thermal imaging," (1994), vol. 2234, pp. 275–286.
3. J. S. Tyo, C. F. LaCasse, and B. M. Ratliff, "Total elimination of sampling errors in polarization imagery obtained with integrated microgrid polarimeters," Opt. Lett. **34**, 3187–3189 (2009).
4. C. F. LaCasse, R. A. Chipman, and J. S. Tyo, "Band limited data reconstruction in modulated polarimeters," Opt. Express **19**, 14976–14989 (2011).
5. C. F. LaCasse, J. S. Tyo, and R. A. Chipman, "Role of the null space of the DRM in the performance of modulated polarimeters," Opt. Lett. **37**, 1097–1099 (2012).
6. D. A. LeMaster and K. Hirakawa, "Improved microgrid arrangement for integrated imaging polarimeters," Opt. Lett. **39**, 1811–1814 (2014).
7. B. M. Ratliff, C. F. LaCasse, and J. S. Tyo, "Interpolation strategies for reducing IFOV artifacts in microgrid polarimeter imagery," Opt. Express **17**, 9112–9125 (2009).
8. A. S. Alenin and J. S. Tyo, "Generalized channeled polarimetry," J. Opt. Soc. Am. A **31**, 1013–1022 (2014).
9. J. S. Tyo, "Design of optimal polarimeters: Maximization of signal-to-noise ratio and minimization of systematic error," Appl. Opt. **41**, 619–630 (2002).
10. C. L. Bradley, M. Kupinski, D. J. Diner, F. Xu, and R. A. Chipman, "Spectral invariance hypothesis study of polarized reflectance with ground-based multiangle spectropolarimetric imager (groundMSPI)," (2015), vol. 9613, pp. 96130U–96130U–9.
11. Z. Wang and A. C. Bovik, "Mean squared error: Love it or leave it? a new look at signal fidelity measures," IEEE Signal Process. Mag. **26**, 98–117 (2009).
12. D. Alleysson, S. Susstrunk and J. Herault, "Linear demosaicing inspired by the human visual system," IEEE Trans. Image Process. **14**, 439–449 (2005).
13. E. Dubois, "Frequency-domain methods for demosaicking of Bayersampled color images," IEEE Signal Process. Lett. **12**, 847–850 (2005).
14. C. LaCasse, T. Ririe, R. Chipman, and J. S. Tyo, "Systems description of measurement and reconstruction of microgrid polarimeters," (2011), pp. 1–8.